TITLE:

Large-scale quantification of human osteocyte lacunar morphological biomarkers as assessed by ultra-high-resolution desktop micro-computed tomography

AUTHORS: Elliott Goff[1], Federica Buccino[1], Chiara Bregoli[1], Jonathan P. McKinley[1,2], Basil Aeppli[1], Robert R. Recker[3], Elizabeth Shane[4], Adi Cohen[4], Gisela Kuhn[1], Ralph Müller[1*]

AFFILIATIONS:

[1] Institute for Biomechanics, ETH Zurich, Zurich, Switzerland

[2] Department of Mechanical Engineering, University of California Berkeley, Berkeley, CA, USA

[3] Department of Medicine, Creighton University Medical Center, Omaha, NE, USA

[4] Department of Medicine, Columbia University College of Physicians & Surgeons, New York, NY, USA

*Corresponding author:

Prof. Ralph Müller, PhD

Institute for Biomechanics, ETH Zurich, Zurich, Switzerland

Leopold-Ruzicka-Weg 4, 8093, Zurich, Switzerland

E: ram@ethz.ch

T: +41 44 632 45 92

ABSTRACT

Ultra-high-resolution imaging of the osteocyte lacuno-canalicular network (LCN) three-dimensionally (3D) in a high-throughput fashion has greatly improved the morphological knowledge about the constituent structures – positioning them as potential biomarkers. Technologies such as serial focused ion beam/scanning electron microscopy (FIB/SEM) and confocal scanning laser microscopy (CLSM) can image in extremely high resolution, yet only capture a small number of lacunae. Synchrotron radiation computed tomography (SR-CT) can image with both high resolution and high throughput but has a limited availability. Desktop micro-computed tomography (micro-CT) provides an attractive balance: high-throughput imaging on the micron level without the restrictions of SR-CT availability. Over the past decade, desktop micro-CT has been used to image osteocyte lacunae in a variety of animals, yet few studies have employed it to image human lacunae using clinical biopsies.

In this study, accuracy, precision, and sensitivity of large-scale quantification of human osteocyte lacunar morphometries were assessed by ultra-high-resolution desktop micro-computed tomography. For this purpose, thirty-one transiliac human bone biopsies containing trabecular and cortical regions were imaged using ultra-high-resolution desktop micro-CT at a nominal isotropic voxel resolution of 1.2µm. The resulting 3D images were segmented, component labeled, and the following morphometric parameters of 7.71 million lacunae were measured: Lacunar number (Lc.N), density (Lc.N/BV), porosity (Lc.TV/BV), volume (Lc.V), surface area (Lc.S), surface area to volume ratio (Lc.S/Lc.V), stretch (Lc.St), oblateness (Lc.Ob), sphericity (Lc.Sr), equancy (Lc.Eq), and angle (Lc.θ).

Accuracy was quantified by comparing automated lacunar segmentation to manual segmentation. Mean true positive rate (TPR), false positive rate (FPR), and false negative rate (FNR) were 89.0%, 3.4%, and 11.0%, respectively. Regarding the reproducibility of lacunar morphometry from repeated measurements, precision errors were low (0.2 – 3.0%) and intraclass correlation coefficients were high (0.960 – 0.999). Significant differences between cortical and trabecular regions

45 ($p<0.001$) existed for Lc.N/BV, Lc.TV/BV, local lacunar surface area (<Lc.S>), and local lacunar volume
46 (<Lc.V>), all of which demonstrate the sensitivity of the method and are possible biomarker
47 candidates. This study provides the rigorous foundation required for future large-scale morphometric
48 studies using ultra-high-resolution desktop micro-CT and high-throughput analysis of millions of
49 osteocyte lacunae in human bone samples. Furthermore, the validation of this technology for
50 imaging of human lacunar properties establishes the quality and reliability required for the accurate,
51 precise, and sensitive assessment of osteocyte morphometry in clinical bone biopsies.

INTRODUCTION

Bone as an organ provides humans with the necessary structural support to sustain locomotion and dynamic movement in daily life. The organ is uniquely capable of adapting its structure to meet the mechanical demands that are placed upon it [1]. This adaptation of bone has been described by Roux as bone (re)modeling [2]. Central to this process are the osteocytes: the most abundant bone cell type, embedded deeply within the bone matrix, and each ensconced within individual compartments called lacunae [2, 3]. Woven together by a large number of dendrites that extend from each cell, the lacuno-canalicular network (LCN) is one of the most intricately connected networks in the human body, and the scale is comparable with the network of neurons in the human brain [4]. Compelling studies over the last thirty years have revealed and emphasized the functional importance of the cells and processes within the LCN to sense mechanical signals, to transduce them into chemical signals, and to orchestrate the bone (re)modeling process through guided bone formation and bone resorption [5-10].

After cell death, the fossilized lacuna remains intact, allowing the lacuna's three-dimensional (3D) geometry to be extracted via several imaging techniques at the sub-micrometer resolution. Today, serial focused ion beam/scanning electron microscopy (FIB/SEM) possesses the highest spatial resolution in the nanometer range. Yet, while this technology allows for features like individual dendritic processes to be resolved, the depth range is a major limitation, and only a few dozen lacunae in the tissue can be captured simultaneously [11-14]. Other researchers have implemented confocal laser scanning microscopy (CLSM) to investigate lacunar geometry in mice [15, 16] and in clinical bone biopsies [17], but again the shallow tissue depth that can be explored is a limitation and hence only small subsections of bone consisting of a few dozen to a few hundred lacunae can be measured with CLSM. Both FIB/SEM and CLSM suffer from a lack of scalability since the time required for a study with more than a few hundred lacunae makes the technologies impractical for any type of large-scale lacunar analysis. Alternatively, several groups have used high-resolution x-ray-based approaches such as synchrotron radiation computed tomography (SR-CT). Several studies, Mader et

al. [18] in particular, have been successful in separating the porous lacunae from the surrounding matrix in a high-throughput fashion in complete intact mouse femurs [18-24]. However, SR-CT is an imaging tool that requires access to a beamline facility, of which only a few in the world exist, and hence the availability is limited for most researchers due to timing restrictions. A fourth imaging tool, conventional x-ray based ultra-high-resolution desktop micro-computed tomography (micro-CT), provides a reasonable balance between CLSM and SR-CT. Ultra-high-resolution desktop micro-CT allows for the extraction of millions of lacunae from complete bone biopsies without the need to request approval for limited time slots or experienced personnel at beamline facilities. Furthermore, desktop micro-CT is an established and validated technology that has been implemented for laboratory-based bone research for several decades [25-28]. Therefore, it is necessary that a technique be developed for large-scale, high-throughput imaging of osteocyte lacunar networks in clinical bone biopsies.

Equally as important as the 3D images acquired are the individual structures that are extracted from these images as well as the accurate, reproducible, and sensitive quantification of their morphometry. Specifically, with ultra-high-resolution osteocyte imaging, it is imperative that the lacunar morphometric parameters are well defined and measured accordingly. Great strides have been made towards the standardization of these metrics in recent years, and several studies have explored different basic measures such as lacunar density, shape, and orientation [18, 20, 21, 29-34]. Mader et al. have most thoroughly described and validated both simple and abstract lacunar morphometric parameters, and hence this study follows their naming convention and mathematical definitions [18]. The combination of well-defined lacunar morphometric parameters and a rigorously validated imaging and analysis methodology allow for the emergence of biomarkers. These morphometric biomarkers have the potential to be used to differentiate between diseased and healthy bone, old and young bone, or even the region of bone within the body.

This study aims to provide researchers with a fully validated method of large-scale lacunar imaging, accurate automated segmentation, and measurements of each resulting 3D lacunar

structure using a technology that is widely accessible – ultra-high-resolution desktop micro-CT. Furthermore, we demonstrate the power of such a high-throughput analysis by measuring the morphometric parameters of millions of osteocyte lacunae in human bone samples, using the previously validated 3D lacunar metrics of Mader et al. [18]. The rigor of the method is confirmed by accurate image segmentation, a standard precision study [35], and the sensitive detection of differences between cortical and trabecular regions. Thorough validation highlights the value of the imaging method, and we believe this study will provide a rigorous foundation for future large-scale lacunar investigations.

METHODS

Human bone biopsy preparation

Thirty-one transiliac bone biopsy samples from premenopausal women already described in previous studies by Cohen et al. [36, 37] were used for this study. Biopsy samples had been obtained in women, aged 18-48, recruited as a reference population for studies of bone structure and metabolism in premenopausal women. Reference population subjects were required to have normal areal spine, hip, and forearm BMD by dual-energy x-ray absorptiometry (DXA; Z score ≥ -1.0 at all sites), no history of adult low trauma fracture, and no historical or biochemical evidence of diseases or conditions known to affect skeletal integrity [36, 37]. All subjects provided written informed consent; studies had been approved by the institutional review boards of all participating institutions.

A hemi-cylinder fraction of each biopsy core, containing both cortical and trabecular regions, was embedded in individual polymethylmethacrylate (PMMA) disks with a 25mm diameter. Subsections of each sample were prepared to fit in the desktop micro-CT scanner, which limits the diameter to a 4.0mm field of view (FOV) in the ultra-high-resolution mode. Hence, each PMMA embedded core was cut three times parallel to the longitudinal axis of the biopsy using a circular

diamond blade (SCAN-DIA Minicut 40, SCAN-DIA GmbH & Co. KG, Germany) and custom-made mounts for sample fixation. This produced a rectangular block, which had the XY target dimensions of 4.25 +/- 0.1mm with the Z dimension depending on the original placement in the PMMA disk and ranging from 20-25mm. Each block was then turned on a conventional lathe (Schaublin 102, Bevilard, Switzerland) to create a final cylinder of 3.8 +/- 0.05mm diameter and a length ranging between 10 and 15mm. The biopsy cylinder was then tightly fit into a custom sample holder as seen in Figure 1 to minimize motion artifacts and to maximize the volume scannable within the 4.0mm diameter FOV.

Image Acquisition

Biopsy subsamples were imaged with a µCT50 (Scanco Medical AG, Brüttisellen, Switzerland), operated with a 0.5mm aluminum filter, 72µA current, 4W power, 55kVp energy, 1.5s integration time, level 6 data averaging, and with a total of 1500 projections. Images were reconstructed at a nominal isotropic voxel resolution of 1.2µm with an anti-ring level 8 to minimize center ring artifacts using the manufacturer's scanner software. Each image consisted of a cylindrical volume equal to the full diameter of the sample (3.8 +/- 0.05mm) and the height of one scan stack (909 slices = 1.09mm). The protocol for each sample consisted of three scans: 1. Prescan to warm the sample in the scanner gantry in an effort to reduce motion artifacts caused by thermal effects (1 hour) 2. Cortical region scan starting from the lowest point on the centerline of the sample and scanning up one stack (10 hours) 3. Trabecular region scan stack in the middle of the biopsy equidistant between both cortical walls (10 hours). A visual example of this scanning protocol and resulting images can be seen in Figure 1.

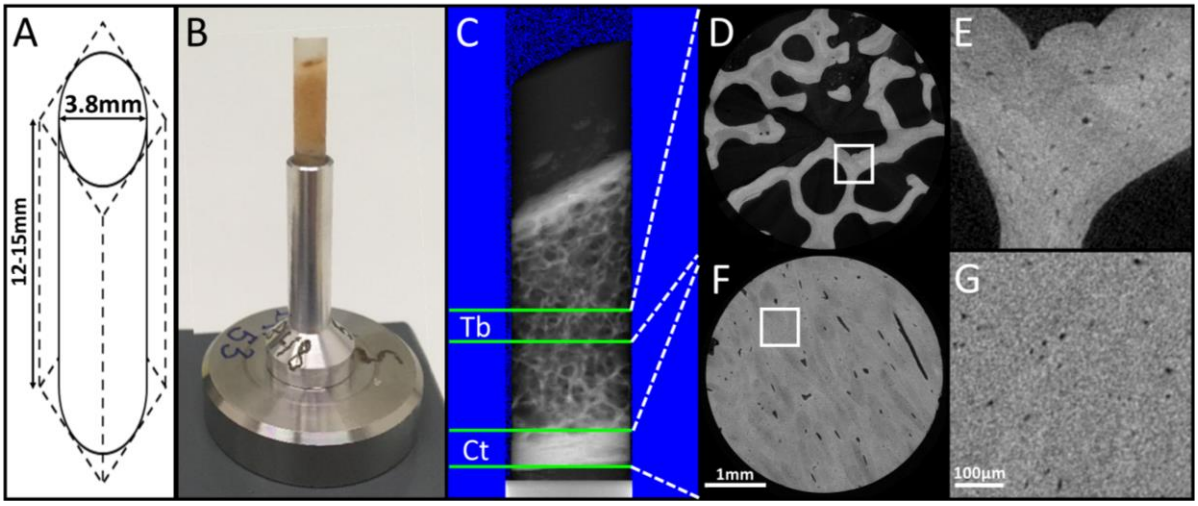

Figure 1: A) Schematic of sample core extraction from hemi-cylinder biopsy, which consisted of three linear cuts followed by a lathe turn. B) Photograph of final machined biopsy core inserted into a tolerance-fit sample holder. C) Scout-view overview of entire sample (XZ plane) with the trabecular (Tb) and cortical (Ct) scanned regions identified between the respectively labeled green lines. D) Ultra-high-resolution micro-CT scan of trabecular region cross-section (XY plane) and E) enlarged trabecular subregion. F) Ultra-high-resolution micro-CT scan of cortical region cross-section (XY plane) and G) enlarged cortical subregion.

To determine the optimal beam energy, three samples of trabecular bone were scanned at three beam energies: 55, 70, and 90kVp. These samples used for beam energy optimization originated from a separate study [38]; however, they were also human bone biopsies from the iliac crest and were considered to be comparable with our biopsy group. We aimed to maximize the image signal-to-noise ratio (SNR) just as previous studies relating to other anatomical bone sites had done [39]. The linear attenuation coefficient (raw signal) was measured for ten two-dimensional sub-regions (~0.25mm^2) at every beam energy in three samples for 90 regions in total. SNR was then calculated by adapting the Firbank equation to account for two distinct materials as described in Equation 1 where μ is the average coefficient of linear attenuation of bone and the background (PMMA) and σ is the standard deviation of the background [40].

$$\mathrm{SNR} = 0.655\frac{\mu_{\mathrm{bone}} - \mu_{\mathrm{PMMA}}}{\sigma_{\mathrm{PMMA}}} \quad (1)$$

Image Preprocessing

Preprocessing of each image consisted of a constrained 3D Gaussian low pass filter (σ=0.8, support =1) to reduce noise and was applied using IPL (Scanco Medical AG, Brüttisellen, Switzerland). Segmentation of lacunar structures was performed by inverting the image after applying a threshold that was individualized for each image volume, which was necessary due to the large variation in tissue mineral density (TMD) distributions between samples at this resolution. The lacunar threshold was determined by fitting a Gaussian distribution to each sample's raw TMD distribution data and calculating the first critical point (g') of the fitted distribution using a custom Python script (3.7.1, Python Software Foundation, Delaware, USA). Bone volume (BV) was determined by fixing a threshold of 520mg HA/ccm, applying to all samples, performing a closing operation, and calculating the resulting BV using IPL software (Scanco Medical AG, Brüttisellen, Switzerland).

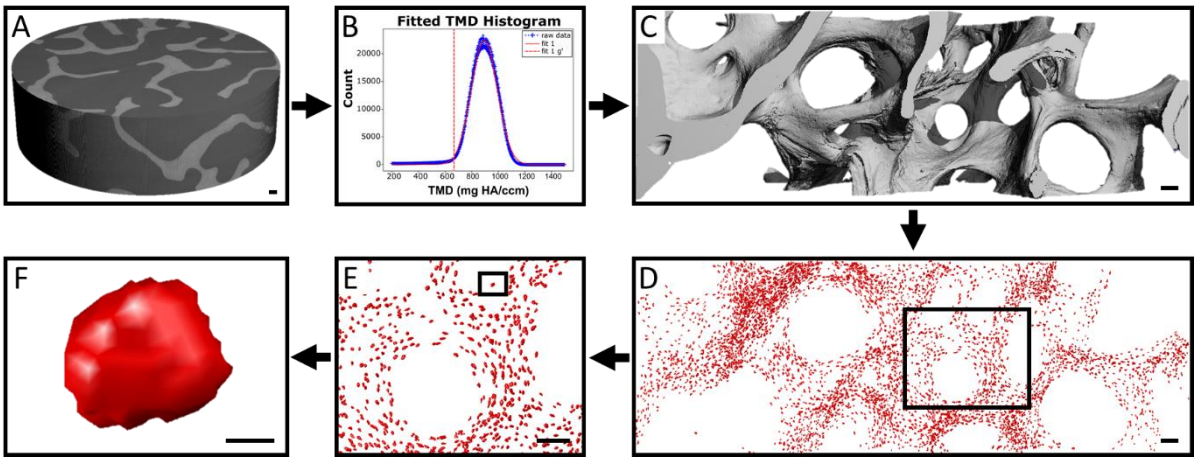

Figure 2: Visual overview of large-scale lacunar segmentation. A) Gaussian filtered, unsegmented, complete micro-CT image stack. B) Sample specific histogram of tissue mineral density (TMD) values fitted by a Gaussian function. A unique lacunar threshold is chosen for each sample at the first critical point of the respective fit by calculating the maximum of the first derivative (g'). C) Lacunar threshold calculated with (B) applied to (A). D) Image (C) inverted and component labeled to identify lacunae. E) Enlarged subregion group of lacunae. F) Single visualized lacuna. Scale bar lengths: A-E) 100μm F) 10μm.

All objects smaller than 50μm^3 and larger than 2000μm^3 were removed as to reflect the range of human lacunar volumes reported in previous histological studies [41]. The lower bound filters out noise structures while the upper bound excludes larger porosities like Haversian and Volkmann canals. Similar volumetric ranges have also been implemented in previous studies [42, 43]. Several microcracks, blood vessels, and image ring artifacts escaped the volumetric filter, yet all

189 exhibited similar thin structures with a high object-elongation value. Therefore, these were excluded
190 by removing all objects with an elongation above a threshold (Lc.St > 0.85). All objects sharing a
191 border with the image edge were also removed to exclude partially cutoff objects.

192 ## Image Morphometry

193 The lacunar morphometries were calculated with a custom Python script, which first
194 component labeled all lacunar objects, applied a surface mesh to each, and then measured basic
195 individual parameters. Lacunar density (Lc.N/BV) was calculated by normalizing the number of
196 lacunae (Lc.N) to the bone volume (BV) and lacunar porosity (Lc.TV/BV) by dividing the total volume
197 of all lacunae by the respective BV. Local parameters (denoted with <> and first defined by Stauber et
198 al. [44]) were each normalized to the sample Lc.N while population-based parameters (denoted with
199 []) were not normalized. Individual lacunar volume (Lc.V), lacunar surface area (Lc.S), and the Eigen
200 vectors were determined from the object specific mesh. This mesh was calculated by performing a
201 triangulation of the surface voxels of the object using Lewiner marching cubes (3.7.1, Python
202 Software Foundation, scikit-image library, Delaware, USA). The Eigen vectors were then used to
203 quantify more complex parameters including lacunar stretch (Lc.St) and lacunar oblateness (Lc.Ob),
204 which were first defined by Mader et al. [18]. Lacunar equancy (Lc.Eq) was the ratio between the
205 smallest and largest Eigen vectors (E3/E1) [21, 45] while lacunar sphericity (Lc.Sr) related the lacunar
206 object to a sphere via the ratio between Lc.S and Lc.V [43]. Lacunar angle (Lc.θ) was measured in
207 degrees and ranged between 0 and 180 degree in relation to an arbitrarily created unit vector that
208 was held consistent between images.

209 ## Validation

210 *Accuracy:*

211 To evaluate the accuracy of the threshold approach, sub-volumes from five samples
212 consisting of roughly 200 lacunae per region were hand-counted by a trained observer and then
213 compared with the automatically segmented data at the corresponding sample-specific g' threshold

to calculate true positive, false positive, and false negative rates (TPR, FPR, FNR). All objects were verified in 3D as depicted in Figure 3 and falsely classified objects were reclassified when appropriate.

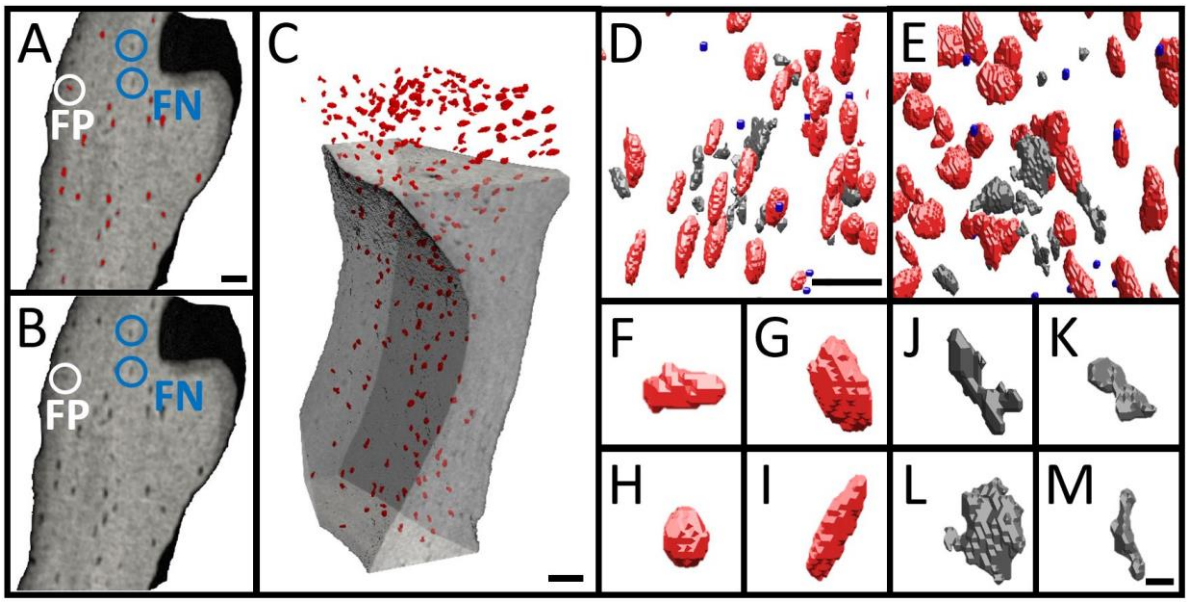

Figure 3: Manual vs. automatic lacunar segmentation. A) 3D cutplane of trabecular subregion with automatically segmented objects highlighted in red. Examples of false negatives (FN) circled in blue, false positives (FP) circled in white. B) Same cutplane as (A) used for visual comparison regarding classification of automatically segmented objects, showing same FP and FN as in (A). C) 3D orthographic projection of (A&B) with automatically segmented objects in red. D&E) 3D visualization comparing manual and automatic lacunar segmentation. Red objects = true positives (TP); objects identified as lacunae both manually and automatically. Gray objects = false positives (FP); objects identified as lacunae automatically but rejected manually. Blue spheres = false negatives (FN); objects manually identified as lacunae but rejected by the automatic method. F-I) TP examples. J-M) FP examples. Scalebar A-E) = 50μm; F-M) = 10μm.

Reproducibility:

In accordance with literature that recommends a sufficient number of degrees of freedom (DOF) to produce an upper confidence limit of the precision error that is 40% greater than the mean precision error [35], six samples were measured five times and repositioned between each measurement for a total of 20 DOF. Reproducibility was evaluated by calculating the precision error

231 ($PE_{\%CV}$) and the intraclass correlation coefficient (ICC) for the measured lacunar indices using

232 Equations 2 – 4.

233 $$PE_{SD} = \sqrt{\sum_{j=1}^{m} \frac{SD_j^2}{m}} \quad (2)$$

234

235 $$PE_{\%CV} = \sqrt{\sum_{j=1}^{m} \frac{\%CV_j^2}{m}} \quad (3)$$

236

237 $$ICC = \frac{F_0 - 1}{F_0 + (n-1)} \quad (4)$$

238 *Sensitivity:*

239 To assess the sensitivity of the method, lacunar morphometric parameters from cortical and

240 trabecular regions were compared as there are known physiological differences between the

241 distribution and shape of lacunae in these regions in humans [43, 46]. Because each individual biopsy

242 contained both cortical and trabecular regions, it was possible to compare lacunae both within

243 samples and between samples.

244 Statistical Analysis

245 A paired t-test with the necessary Bonferroni correction was performed with respect to

246 energy-dependent imaging parameters in Table 1. With respect to the precision test, the 95%

247 confidence interval was calculated for each morphometric parameter using a chi-squared distribution

248 to gain an understanding of certainty with respect to the PE and ICC reported values in Table 3.

249 Creating two-parameter plots of the data presented in Table 3 is another way to evaluate the

250 reproducibility of the imaging method by means of clustering as is depicted in Figure 5. A paired

Student's t-test was performed to evaluate regional differences between lacunar parameters that were normalized to tissue indices ($p<0.001$). Population-based parameters were not normally distributed following a Kolmogorov-Smirnov test, and so a non-parametric Mann-Whitney U test was performed to evaluate population differences ($p<0.001$). The inter-quartile ranges and medians were computed for each morphometric parameter.

RESULTS

Image Acquisition

Images captured with a 55kVp beam energy exhibited a significantly higher SNR when compared to images obtained with a beam energy of 90kVp ($p<0.005$). The SNR measured with the 70kVp beam energy fell in between the high and low beam energy values and did not differ significantly from the other energies.

Table 1: Energy dependency of imaging parameters. Energy level 55kVp used as baseline and paired t-test with the necessary Bonferroni correction used to test for significant differences between energy levels in the three following categories: contrast, standard deviation of the image background (σ_{PMMA}), and signal-to-noise ratio (SNR). Significantly different ($p<0.005$) from baseline denoted with (*) and from 70kVp with (#).

Energy (kVp)	Contrast (n=30)	σ_{PMMA} (n=30)	SNR (n=30)
55	1.84±0.46	0.14±0.02	8.34±2.20
70	1.33±0.33*	0.11±0.01*	7.65±1.88
90	0.92±0.23*#	0.09±0.01*#	6.67±1.60*

As shown in Table 1, both contrast and standard deviation of the background (PMMA in this case) were inversely proportional to the beam energy. Specifically, the inverse proportionality was approximately linear with contrast while σ_{PMMA} was quadratic (Figure 4), both important for the

computation of SNR as given in Equation 1. As a ratio of both noise and the standard deviation of the image background (Equation 1), SNR was less dramatically affected by increasing beam energy. We therefore set the beam energy to 55kVp for all scans in the study because this setting produced the highest quality images with the highest contrast at acceptable noise levels.

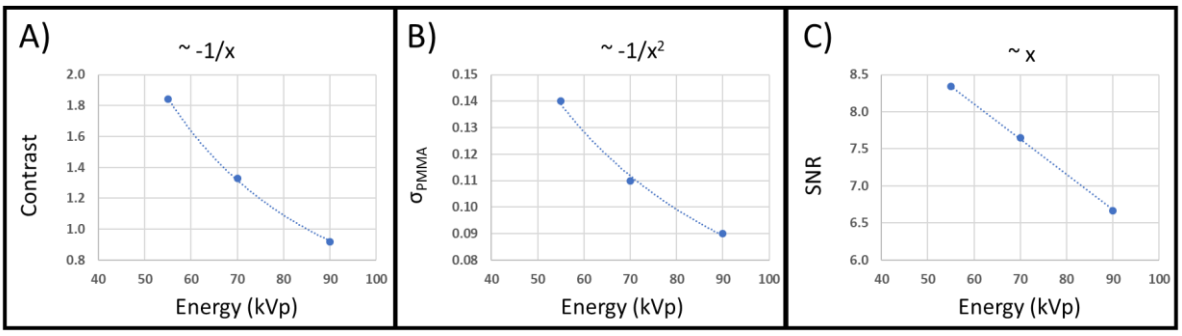

Figure 4: Beam physics relationships. A) Contrast exhibits an inverse relationship with beam energy. B) Standard deviation of the background (σ_{PMMA}) has an approximate quadratic relationship with beam energy. C) Signal-to-noise ratio is linearly related to beam energy as expected since it is defined as the contrast divided by the σ_{PMMA}.

Validation

Accuracy:

Automated segmented objects were compared to the manual segmentation to evaluate TPR, FPR, and FNR measures as seen in Table 2. Objects segmented automatically in each sample revealed a strong agreement with the lacunae counted manually as is evident by the high TPR and low FPR and low FNR. Roughly 200 lacunae were present in each sample subregion with sample 1 exhibiting the highest TPR (93.9%) and lowest FNR (6.1%). Sample 4 had the lowest FPR (0.5%) while sample 3 the lowest TPR (77.3%). The final accuracy measure was calculated as the mean of the five samples and was computed to be 89.0% TPR, 3.4% FPR, and 11.0% FNR.

Table 2: Quantification of accuracy measures and their corresponding rates obtained via comparison between manual and automatic lacunar segmentation methods. TPR = True Positive Rate; FPR = False Positive Rate; FNR = False Negative Rate.

Sample	TP	FP	FN	TPR (%)	FPR (%)	FNR (%)
1	155	9	10	93.9	5.5	6.1
2	182	11	14	92.9	5.7	7.1
3	133	3	39	77.3	2.2	22.7
4	202	1	16	92.7	0.5	7.3
5	205	7	27	88.4	3.3	11.6
Mean	175	6	21	89.0	3.4	11.0

Reproducibility:

Measurement repeatability is crucial for validation and was quantified for measured lacunae. Across all lacunar morphometric parameters, precision errors were very low (below 3%) and the ICC were very high (above 0.980), which indicate that these lacunar measurements are extremely reproducible. The 95% confidence interval range for precision errors was between 0.67% and 3.68% while the range for ICC values were between 0.883 and 1.000, which indicates extremely low measurement variability and high reproducibility.

Table 3: Reported values from the reproducibility analysis (n=6, five repeated measurements). Morphometric parameters include: lacunar total volume (Lc.TV), lacunar porosity (Lc.TV/BV), lacunar number (Lc.N), lacunar density (Lc.N/BV), local lacunar volume (<Lc.V>), local lacunar surface area (<Lc.S>), local lacunar stretch (<Lc.St>), local lacunar oblateness (<Lc.Ob>), local lacunar sphericity (<Lc.Sr>), local lacunar equancy (<Lc.Eq>), and local lacunar angle (<Lc.θ>). In addition to mean values of each morphometric parameter across the samples, we report the following for precision errors (PE): standard deviation (PE_{SD}) in absolute values, coefficient of variation ($PE_{\%CV}$) of the repeated experiments, and the 95% confidence interval of the variation (95% CI $PE_{\%CV}$). Also reported are the intraclass correlation coefficients (ICC) and the 95% confidence interval of the ICC for each respective morphometric parameter.

Morphometric parameter	Mean	PE_{SD}	$PE_{\%CV}$	95% CI $PE_{\%CV}$	ICC	95% CI ICC
Lc.TV (1000*µm³)	2,119.3	40.2	2.77%	2.11-4.05%	0.997	0.992-1.000
Lc.TV/BV (%)	0.5	0.009	2.52%	1.91-3.68%	0.989	0.966-0.998
Lc.N (1000)	10.03	0.2	1.86%	1.41-2.72%	0.999	0.996-1.000
Lc.N/BV (1000/mm³)	22.09	0.3	1.48%	1.12-2.16%	0.984	0.952-0.997
<Lc.V> (µm³)	210.5	2.5	1.33%	1.01-1.95%	0.991	0.970-0.999
<Lc.S> (µm²)	207.5	1.7	0.88%	0.67-1.29%	0.990	0.968-0.998
<Lc.St> (1)	0.6	0.001	0.17%	0.13-0.25%	0.989	0.963-0.998
<Lc.Ob> (1)	-0.4	0.006	1.59%	1.21-2.32%	0.960	0.883-0.994
<Lc.Sr> (1)	0.8	0.002	0.24%	0.18-0.35%	0.938	0.816-0.990
<Lc.Eq> (1)	0.3	0.001	0.43%	0.33-0.63%	0.994	0.980-0.999
<Lc.θ> (Degree)	113.8	0.8	0.66%	0.50-0.97%	0.980	0.938-0.997

Clustering of the individual repeated measurements indicates reproducibility and is especially apparent in Figure 5A-B. These parameters also exhibited a very high correlation, which illustrated that as bone volume increases so will the number of lacunae and the total lacunar volume. The clustering in Figure 5C-D was not nearly as evident across all six samples due to the fact that <Lc.V> and <Lc.St> were more difficult to reproduce. As BV/TV increases in Figure 5C-D, measured variability decreases between the first and second cluster and then remains approximately constant. The strong correlation of Lc.N (R^2 = 0.99) and Lc.TV (R^2 = 0.98) with BV/TV position them as potential lacunar

biomarker candidates. <Lc.V> and <Lc.St> were more independent of BV/TV and no correlation was found.

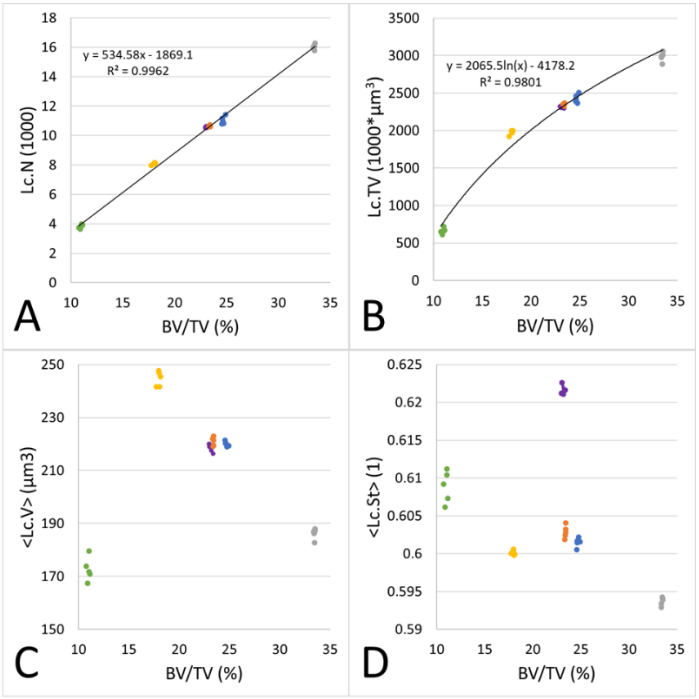

Figure 5: Two-parameter plots that demonstrate the reproducibility of the imaging method. Each color represents an individual sample and each data point represents a specific measurement (n=6, with 5 repeated measurements). A) Lacunar number (Lc.N) vs. bone volume (BV/TV). B) Lacunar total volume (Lc.TV) vs. bone volume (BV/TV). C) Local lacunar volume (<Lc.V>) vs. bone volume (BV/TV). D) Local lacunar stretch (<Lc.St>) vs. bone volume (BV/TV).

Sensitivity:

Cortical and trabecular bone regions were measured and compared. More bone was present, and consequently, more lacunae were present in cortical bone when compared to trabecular bone. Measured tissue values such as BV, and BV/TV in trabecular regions were consistently lower than cortical regions as expected since trabecular bone is sparse and cortical bone is compact. Regarding the global morphometries, which were normally distributed, Lc.N/BV median value in trabecular bone was nearly half of what it was observed to be in cortical bone (16,611 vs. 26,429, $p<0.001$). Similarly, the median value of Lc.TV/BV in trabecular bone was also nearly half of what it was in

cortical bone (0.30% vs. 0.58%, $p<0.001$), again indicating that cortical bone has a significantly higher lacunar porosity than trabecular bone. Furthermore, we report in Table 4 that the normalized local parameters <Lc.V> and <Lc.S> are significantly greater ($p<0.001$) in cortical bone (<Lc.V> = 223μm^3; <Lc.S> = 233μm^2) than in trabecular bone (<Lc.V> = 178μm^3; <Lc.S> = 194μm^2). Most population-based morphometric parameters were not normally distributed, and consequently we reported the median values as well as the interquartile range for all indices to provide a sense of the distribution of each parameter in Table 4.

Table 4: Large-scale lacunar morphometric parameters (n=6.57 million for cortical and n=1.14 million for trabecular). Reported values are the median with interquartile range (25th percentile – 75th percentile). Morphometric parameters include: total image volume (TV), total bone volume (BV), ratio of bone volume to total volume (BV/TV), lacunar porosity (Lc.TV/BV), lacunar number (Lc.N), lacunar density (Lc.N/BV), local lacunar volume (<Lc.V>), local lacunar surface area (<Lc.S>), population lacunar volume ([Lc.V]), population lacunar surface area ([Lc.S]), population lacunar surface area to volume ratio ([Lc.S/Lc.V]), population lacunar stretch ([Lc.St]), population lacunar oblateness ([Lc.Ob]), population lacunar sphericity ([Lc.Sr]), population lacunar equancy ([Lc.Eq]), and population lacunar angle ([Lc.θ]). Paired t-test performed for the normally distributed global and local parameters, (*) indicates p<0.001. Mann-Whitney U test performed on population-based parameters and (*) indicates p<0.001.

Morphometric parameter	Trabecular	Cortical
TV (mm^3)	15.7 (15.1–15.8)	15.7 (15.6–15.9)
BV (mm^3)	2.11 (1.54–2.46)*	7.68 (6.33–9.70)
BV/TV (%)	14.0 (10.2–18.4)*	57.8 (43.7–64.9)
Lc.TV/BV (%)	0.30 (0.22–0.38)*	0.58 (0.51–0.65)
Lc.N (1000)	41.2 (27.7–67.9)*	252 (175–266)
Lc.N/BV (1000/mm^3)	16.6 (14.1–18.7)*	26.4 (23.7–29.3)
<Lc.V> (μm^3)	178 (159–197)*	223 (189–245)
<Lc.S> (μm^2)	194 (178–211)*	233 (216–248)
[Lc.V] (μm^3)	123 (70.1–230)*	116 (63.0–272)
[Lc.S] (μm^2)	161 (109–245)*	164 (105–290)
[Lc.S]/[Lc.V] (1/μm)	1.30 (1.05–1.56)*	1.41 (1.06–1.66)

[Lc.St] (1)	0.62 (0.53–0.69)*	0.61 (0.51–0.69)
[Lc.Ob] (1)	-0.44 (-0.67– -0.13)*	-0.49 (-0.71– -0.17)
[Lc.Sr] (1)	0.76 (0.70–0.81)*	0.73 (0.66–0.79)
[Lc.Eq] (1)	0.29 (0.19–0.45)*	0.31 (0.19–0.47)
[Lc.θ] (Degree)	104 (76.0–131)*	107 (77.4–134)

Population-based lacunar parameters were not normally distributed. The interquartile ranges between regions were similar, yet a non-parametric Mann-Whitney U test revealed significant differences between cortical and trabecular regions ($p<0.001$). The measure of sphericity ([Lc.Sr]) was approximately 0.75 for both regions of bone, indicating similarities between the measured ellipsoids and an idealized sphere. The additional parameters [Lc.Eq], [Lc.St] and [Lc.Ob] allow for the ellipsoidal lacunar shape to be described in more detail, and the median reported values suggest that these are indeed ellipsoidal structures in both trabecular and cortical regions. The range of [Lc.Ob] in trabecular bone was slightly higher than in cortical bone.

Figure 6 depicts selected global, local, and population-based morphometries from both cortical and trabecular regions. When normalized to the analyzed tissue volume, both the lacunar density and porosity were significantly different between cortical and trabecular regions (Figure 6A-B) across all 31 samples, further supporting their potential as biomarkers. Local morphometries (<Lc.V> & <Lc.S>) were also significantly different between the two regions (Figure 6C-D), yet not as clearly separated as the global morphometries. Population-based morphometries (Figure 6E-F) included all lacunar observations across all 31 samples: 1.14 million lacunae in trabecular bone and 6.57 million lacunae in cortical bone. The shape indices [Lc.St] and [Lc.Sr] were chosen to compare between regions and were also significantly different. A visual comparison is presented in Figure 6G-H between the samples containing the median Lc.N/BV values from Figure 6A, further illustrating the differences between regions.

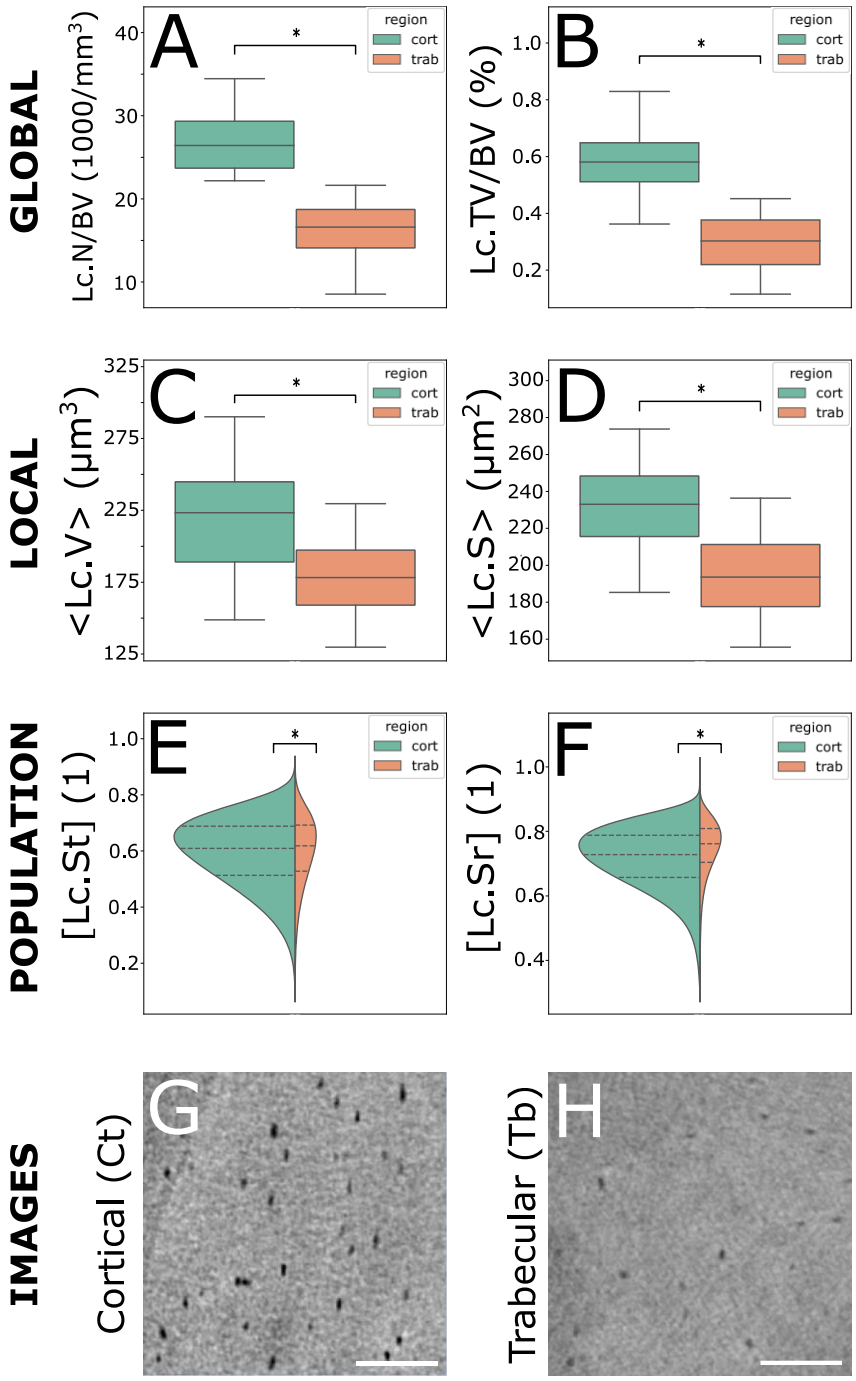

Figure 6: Comparison of cortical and trabecular regions regarding lacunar morphometric parameters. Included in the analysis were 31 samples which comprised of 6.57 million cortical lacunae and 1.14 million trabecular lacunae. A) Lacunar density (Lc.N/BV). B) Lacunar porosity (Lc.TV/BV). C) Local lacunar volume (<Lc.V>) normalized to sample. D) Local lacunar surface area (<Lc.S>) normalized to sample. E) Population-based local lacunar stretch ([Lc.St]) not normalized to sample. F) Population-based local lacunar stretch ([Lc.Sr]) not normalized to sample. G&H) Micro-CT images from cortical and trabecular regions representing the median

values from plot (A) respectively, scale bar = 100μm. Paired t-test performed on normalized parameter plots (A-D) and (*) indicates p<0.001. Mann-Whitney U test performed on population-based parameters (E-F) and (*) indicates p<0.001.

DISCUSSION

Detailed examination of the LCN on a large scale demands a high-resolution 3D-imaging methodology that is accurate, reproducible, and sensitive. Lacunae must be segmented and morphometric indices measured accurately and repeatably. Therefore, it is paramount that researchers select a fully validated imaging methodology for the large-scale assessment of osteocyte lacunar morphometry. High-resolution desktop micro-CT is an ideal technology for large-scale investigation of the lacunar network due to its wide accessibility. Micro-CT has been employed for decades as a standard technology for bone tissue morphometry with nominal voxel resolutions in the range of 10-40μm [25-28]. However, this technology has evolved in recent years, and with it, the ability to image higher resolutions on the order of 1μm [47]. Hence, the development of validated image acquisition, processing, and analysis tools to image lacunar morphometry is a logical progression of the science as well as being crucial to understanding the biological impact of the LCN on bone at other hierarchical levels.

Segmenting the lacunar structures from the surrounding mineralized bone matrix required the careful selection of the threshold applied to the image. Typically, a single threshold is chosen by the user via visual inspection and then applied to all samples in a study. At the tissue level this method is acceptable when recommended guidelines are carefully followed [48] and was how BV was calculated in this study. However, due to the wide variation of the TMD distributions between samples at the 1.2μm resolution, this single-threshold method cannot be applied to all samples when imaging lacunae (Figure S1). Therefore, our approach was to pragmatically locate a threshold that was intrinsically linked to the sample specific TMD distribution, compare the resulting segmentation with manual segmentation, and quantify the accuracy. Previous studies have tried similar individual

threshold approaches, which are offset from a reference point of the TMD histogram such as the mean [49], but we found our specific images responded best to selecting the TMD histogram critical point for segmentation (Figure S1). While no single segmentation threshold was able to capture all lacunar structures, the visual comparison in Figure 3 is strikingly good. Alternative descriptors of the TMD distribution were investigated such as the width of the distribution but did not prove to be as effective as the first critical point (Figure S2).

The range of considered object volumes was also important for lacunar segmentation. This range varies substantially between studies and could be as narrow as 50-610μm^3 or as wide as 175-2000μm^3 [18, 21, 42, 43, 50, 51]. Previous examinations of histological slides have estimated the human lacunae to be between 28μm^3 and 1713μm^3, yet lacunae observed below 50μm^3 were only found in fracture callus [41]. After evaluating several different volume ranges and comparing both qualitatively with 2D and 3D images and quantitatively with accuracy measures such as TPR, FPR, and FNR, we determined a lower limit of 50μm^3 to be optimal for lacunar segmentation in human trabecular and cortical bone [52]. The upper limit was chosen to be 2000μm^3 in line with a similar study [21]. This range has a large impact on the number of lacunae segmented and is particularly sensitive on the lower limit. This problem is especially pronounced with respect to desktop micro-CT due to the limited photon count of its X-ray beam technology. Relative to studies conducted with synchrotron CT systems [18, 42], the desktop micro-CT X-ray beam creates image projections with fewer photons, which increases the resulting noise, reduces the image quality, and makes visualization of small lacunae more difficult. A Gaussian filter with a low sigma value of 0.8 was applied so noise would be reduced while the borders of the lacunae would not be blurred beyond the recognition of a trained human observer. Several extremely elongated ring artifacts were observed in segmentations and were successfully removed by implementing an anti-ring reconstruction filter and applying a shape filter that removed objects with a Lc.St value greater than 0.85 [53].

We used ultra-high-resolution desktop micro-CT to image 7.71 million osteocyte lacunae across cortical and trabecular regions in 31 human iliac crest biopsies. We have observed that morphometric differences exist between lacunae in cortical and trabecular regions of bone, which has also been shown in previous studies [43, 46]. Currently, only Akhter et al. [43] have reported sample matched trabecular and cortical lacunar morphometric parameters in human iliac crest biopsies. In contrast to their study, we report higher values of Lc.N/BV and Lc.TV/BV in cortical bone when compared to trabecular bone. However, the narrow volume range they evaluate (50-610μm) and their analysis of less than 1% of the number of lacunae that we examine severely limits the range of variation that they could potentially consider. Additionally, we have proven our desktop micro-CT imaging technique to be accurate, reproducible, and sensitive.

We evaluated not only global lacunar parameters related to tissue measures (Figure 6A-B), but also local (Figure 6C-D) and population-based (Figure 6E-F) values. Population-based morphometry was not normalized and presents the reader with an undistorted perspective of the natural variation of certain morphometric indices across millions of lacunae (Figure 6E-F). This further illustrates the method's sensitivity that we see in Figures 6A-D and also demonstrates the method's ability to capture the natural variation of lacunae in a large-scale analysis.

Manual segmentation was used as our gold-standard for calculating accuracy, because registration between micro-CT images and typical morphological gold-standards like histology is extremely difficult. However, we were careful to create the best manual segmentation dataset possible for comparison. Hernandez et al. have used similar accuracy comparisons in previous studies and in fact, achieve similar rates of TP, FP and FN to ours [49]. Interestingly, sample 3 in our accuracy calculation exhibited an inordinately low TPR and high FNR. This was due to a suboptimal selection of the sample's subregion near the bone surface, which made manual identification of lacunae slightly more difficult.

We observed very low precision errors and high intraclass correlation coefficients with respect to our five consecutive measurements of six samples. These values were in the same range as in the study of Hemmatian et al. who investigated the reproducibility of desktop micro-CT for imaging murine lacunae [47]. The tight clustering of data points when creating two-parameter plots as seen in Figure 5 further proves the reproducibility of the method. Figure 5A and 5B both exhibit tight clustering within the measurements for each sample which is what we expect when comparing lacunar parameters with tissue values like BV/TV. Bone tissue volume is a quantity that micro-CT is excellent at measuring and hence we would expect it to be extremely reproducible. Physiologically speaking, we would also expect Lc.N and Lc.TV to increase with increasing total bone volume, which explains the strong correlation, further adds credibility to the imaging modality, and even positions the two lacunar parameters as potential biomarker candidates. Yet in Figure 5C and 5D, we note that the values of each sample are slightly less clustered in comparison and are not correlated. More specifically, we note that BV/TV remains very consistent but the <Lc.V> and <Lc.St> varies. Small objects are more difficult to mesh and both <Lc.V> and <Lc.St> are dependent on the object mesh which would explain the difficulties with reproduction in comparison to Lc.N and Lc.TV. Hemmatian et al. also found lacunar measures such as <Lc.V> to be less reproducible than tissue measures such as BV/TV [47]. Consequently, <Lc.V> and <Lc.St> do not appear to be good biomarker candidates.

Previous studies have demonstrated that lacunar morphometric parameters differ between trabecular and cortical regions of bone [43, 46]. We used this fact to evaluate the sensitivity of our method by the ability to differentiate lacunae between regions. We report significant differences between global, local, and population-based parameters including Lc.TV/BV, Lc.N/BV, <Lc.V>, <Lc.S>, [Lc.St], and [Lc.Sr] as seen in Table 4 and Figures 6A-F. Furthermore, Figures 6G-H provide a visual confirmation of the difference that we report in Figure 6A. Not only do we see that lacunar density is lower in trabecular regions, but also the lacunae themselves look to be slightly smaller relative to the cortical regions. This would indicate that lacunae in trabecular regions also consist of lower total porosity (Lc.TV/BV), volume (<Lc.V>), and surface area (<Lc.S>). These visual differences further

support our claim that the method is sensitive and reflects the statistically significant differences that we report in Figures 6A-D.

The largest limitation of this study was the inability to compare extracted lacunar morphometry from our ultra-high-resolution desktop micro-CT images with a higher resolution technology such as FIB/SEM. This would have allowed for an accuracy measure not only with respect to the lacunae segmented, but also the accuracy of morphometric parameters such as <Lc.V> and <Lc.S>. Additionally, the segmented lacunar data was very sensitive to the selection of the lower volumetric bound. This was difficult to select since volumetric data from previous studies regarding the distinction between a lacuna and a micropore is limited. Finally, the precision study required weeks of scanning time and consequently was only performed on trabecular bone.

CONCLUSION

We present a new, and rigorously validated high-throughput method to assess osteocyte lacunar morphometry in human bone samples. We use ultra-high-resolution desktop micro-CT, an individualized histogram-based segmentation procedure, and a custom evaluation algorithm to calculate global and local morphometric parameters of 7.71 million lacunae in two distinct regions of 31 human iliac crest bone samples, revealing two potential biomarkers. The validation of our method demonstrates high degrees of accuracy, precision, and sensitivity. Therefore, our new image acquisition and evaluation methodologies greatly expand the number of investigable hypotheses surrounding osteocyte lacunae, while simultaneously employing a widely accessible and mature imaging technology – desktop micro-CT.

ACKNOWLEDGEMENTS

The authors would like to thank the Joint Scoliosis Research Center of The Chinese University of Hong Kong and Nanjing University, Hong Kong & Nanjing, China for their joint efforts on providing and processing the bone biopsies used for beam energy optimization. We would also like to thank Peter Schwilch for assisting with biopsy machining and Dr. Patrik Christen for his mentoring.

REFERENCES

[1] J. Wolff, Das Gesetz der Transformation der Knochen, DMW-Deutsche Medizinische Wochenschrift 19(47) (1892) 1222-1224.
[2] W. Roux, Der Kampf der Theile im Organismus: ein Beitrag zur Vervollständigung der mechanischen Zweckmässigkeitslehre, W. Engelmann1881.
[3] L.F. Bonewald, The amazing osteocyte, J Bone Miner Res 26(2) (2011) 229-38.
[4] P.R. Buenzli, N.A. Sims, Quantifying the osteocyte network in the human skeleton, Bone 75(79) (2015) 144-50.
[5] J. Gluhak-Heinrich, L. Ye, L.F. Bonewald, J.Q. Feng, M. MacDougall, S.E. Harris, D. Pavlin, Mechanical loading stimulates dentin matrix protein 1 (DMP1) expression in osteocytes in vivo, J Bone Miner Res 18(5) (2003) 807-17.
[6] A.G. Robling, P.J. Niziolek, L.A. Baldridge, K.W. Condon, M.R. Allen, I. Alam, S.M. Mantila, J. Gluhak-Heinrich, T.M. Bellido, S.E. Harris, C.H. Turner, Mechanical stimulation of bone in vivo reduces osteocyte expression of Sost/sclerostin, J Biol Chem 283(9) (2008) 5866-75.
[7] T.M. Skerry, L. Bitensky, J. Chayen, L.E. Lanyon, Early strain-related changes in enzyme activity in osteocytes following bone loading in vivo, J Bone Miner Res 4(5) (1989) 783-8.
[8] L. Lanyon, Osteocytes, strain detection, bone modeling and remodeling, Calcified tissue international 53(1) (1993) S102-S107.
[9] F.A. Schulte, D. Ruffoni, F.M. Lambers, D. Christen, D.J. Webster, G. Kuhn, R. Müller, Local mechanical stimuli regulate bone formation and resorption in mice at the tissue level, PLoS One 8(4) (2013) e62172.
[10] R. Huiskes, R. Ruimerman, G.H. van Lenthe, J.D. Janssen, Effects of mechanical forces on maintenance and adaptation of form in trabecular bone, Nature 405(6787) (2000) 704-6.
[11] S. Hirose, M. Li, T. Kojima, P. Henrique, L. de Freitas, S. Ubaidus, K. Oda, C. Saito, N. Amizuka, A histological assessment on the distribution of the osteocytic lacunar canalicular system using silver staining, J. Bone Miner. Metab. 25(6) (2007) 374-382.
[12] C. Palumbo, A 3-dimensional ultrastructural-study of osteoid-osteocytes in the tibia of chick-embryos, Cell Tissue Res. 246(1) (1986) 125-131.
[13] G. Marotti, F. Remaggi, D. Zaffe, Quantitative investigation on osteocyte canaliculi in human compact and spongy bone, Bone 6(5) (1985) 335-337.
[14] D.J. Kubek, V.H. Gattone, M.R. Allen, Methodological Assessment of Acid-Etching for Visualizing the Osteocyte Lacunar-Canalicular Networks Using Scanning Electron Microscopy, Microsc. Res. Tech. 73(3) (2010) 182-186.
[15] C.M. Heveran, A. Rauff, K.B. King, R.D. Carpenter, V.L. Ferguson, A new open-source tool for measuring 3D osteocyte lacunar geometries from confocal laser scanning microscopy reveals age-related changes to lacunar size and shape in cortical mouse bone, Bone 110 (2018) 115-127.
[16] X.H. Lai, C. Price, S. Modla, W.R. Thompson, J. Caplan, C.B. Kirn-Safran, L.Y. Wang, The dependences of osteocyte network on bone compartment, age, and disease, Bone Res. 3 (2015) 11.

[17] F. Repp, P. Kollmannsberger, A. Roschger, M. Kerschnitzki, A. Berzlanovich, G.M. Gruber, P. Roschger, W. Wagermaier, R. Weinkamer, Spatial heterogeneity in the canalicular density of the osteocyte network in human osteons, Bone reports 6 (2017) 101-108.
[18] K.S. Mader, P. Schneider, R. Müller, M. Stampanoni, A quantitative framework for the 3D characterization of the osteocyte lacunar system, Bone 57(1) (2013) 142-54.
[19] M.G. Ascenzi, J. Gill, A. Lomovtsev, Orientation of collagen at the osteocyte lacunae in human secondary osteons, Journal of Biomechanics 41(16) (2008) 3426-3435.
[20] H.M. Britz, Y. Carter, J. Jokihaara, O.V. Leppanen, T.L.N. Jarvinen, G. Belev, D.M.L. Cooper, Prolonged unloading in growing rats reduces cortical osteocyte lacunar density and volume in the distal tibia, Bone 51(5) (2012) 913-919.
[21] Y. Carter, C.D.L. Thomas, J.G. Clement, A.G. Peele, K. Hannah, D.M.L. Cooper, Variation in osteocyte lacunar morphology and density in the human femur - a synchrotron radiation micro-CT study, Bone 52(1) (2013) 126-132.
[22] P. Schneider, M. Meier, R. Wepf, R. Müller, Towards quantitative 3D imaging of the osteocyte lacuno-canalicular network, Bone 47(5) (2010) 848-858.
[23] M. Langer, A. Pacureanu, H. Suhonen, Q. Grimal, P. Cloetens, F. Peyrin, X-Ray Phase Nanotomography Resolves the 3D Human Bone Ultrastructure, Plos One 7(8) (2012) 7.
[24] M. Kerschnitzki, W. Wagermaier, P. Roschger, J. Seto, R. Shahar, G.N. Duda, S. Mundlos, P. Fratzl, The organization of the osteocyte network mirrors the extracellular matrix orientation in bone, J Struct Biol 173(2) (2011) 303-311.
[25] L.P. Bakalova, C.M. Andreasen, J.S. Thomsen, A. Bruel, E.M. Hauge, B.J. Kiil, J.M. Delaisse, T.L. Andersen, D.M. Ph, Relating Intracortical Bone Mechanics to Pore Morphology and Remodeling Characteristics in the Human Fibula, J Bone Miner Res (2018).
[26] M.L. Bouxsein, S.K. Boyd, B.A. Christiansen, R.E. Guldberg, K.J. Jepsen, R. Müller, Guidelines for Assessment of Bone Microstructure in Rodents Using Micro-Computed Tomography, Journal of Bone and Mineral Research 25(7) (2010) 1468-1486.
[27] T. Hildebrand, A. Laib, R. Müller, J. Dequeker, P. Ruegsegger, Direct three-dimensional morphometric analysis of human cancellous bone: Microstructural data from spine, femur, iliac crest, and calcaneus, Journal of Bone and Mineral Research 14(7) (1999) 1167-1174.
[28] R. Müller, H. Van Campenhout, B. Van Damme, G. Van Der Perre, J. Dequeker, T. Hildebrand, P. Ruegsegger, Morphometric analysis of human bone biopsies: A quantitative structural comparison of histological sections and micro-computed tomography, Bone 23(1) (1998) 59-66.
[29] P. Schneider, M. Stauber, R. Voide, M. Stampanoni, L.R. Donahue, R. Müller, Ultrastructural properties in cortical bone vary greatly in two inbred strains of mice as assessed by synchrotron light based micro- and Nano-CT, Journal of Bone and Mineral Research 22(10) (2007) 1557-1570.
[30] Y. Sugawara, H. Kamioka, T. Honjo, K. Tezuka, T. Takano-Yamamoto, Three-dimensional reconstruction of chick calvarial osteocytes and their cell processes using confocal microscopy, Bone 36(5) (2005) 877-883.
[31] R.P. van Hove, P.A. Nolte, A. Vatsa, C.M. Semeins, P.L. Salmon, T.H. Smit, J. Klein-Nulend, Osteocyte morphology in human tibiae of different bone pathologies with different bone mineral density - Is there a role for mechanosensing?, Bone 45(2) (2009) 321-329.
[32] A. Vatsa, R.G. Breuls, C.M. Semeins, P.L. Salmon, T.H. Smit, J. Klein-Nulend, Osteocyte morphology in fibula and calvaria - Is there a role for mechanosensing?, Bone 43(3) (2008) 452-458.
[33] S. Suniaga, T. Rolvien, A. vom Scheidt, I.A.K. Fiedler, H.A. Bale, A. Huysseune, P.E. Witten, M. Amling, B. Busse, Increased mechanical loading through controlled swimming exercise induces bone formation and mineralization in adult zebrafish, Sci Rep 8 (2018) 13.
[34] B. Ay, K. Parolia, R.S. Liddell, Y.S. Qiu, G. Grasselli, D.M.L. Cooper, J.E. Davies, Hyperglycemia compromises Rat Cortical Bone by Increasing Osteocyte Lacunar Density and Decreasing Vascular Canal Volume, Commun. Biol. 3(1) (2020) 9.
[35] C.-C. Glüer, G. Blake, Y. Lu, B. Blunt, M. Jergas, H. Genant, Accurate assessment of precision errors: how to measure the reproducibility of bone densitometry techniques, Osteoporosis International 5(4) (1995) 262-270.

[36] A. Cohen, D.W. Dempster, R.R. Recker, E.M. Stein, J.M. Lappe, H. Zhou, A.J. Wirth, G.H. van Lenthe, T. Kohler, A. Zwahlen, R. Müller, C.J. Rosen, S. Cremers, T.L. Nickolas, D.J. McMahon, H. Rogers, R.B. Staron, J. LeMaster, E. Shane, Abnormal bone microarchitecture and evidence of osteoblast dysfunction in premenopausal women with idiopathic osteoporosis, J Clin Endocrinol Metab 96(10) (2011) 3095-105.

[37] A. Cohen, R.R. Recker, J. Lappe, D.W. Dempster, S. Cremers, D.J. McMahon, E.M. Stein, J. Fleischer, C.J. Rosen, H. Rogers, R.B. Staron, J. Lemaster, E. Shane, Premenopausal women with idiopathic low-trauma fractures and/or low bone mineral density, Osteoporos Int 23(1) (2012) 171-82.

[38] H.X. Chen, J.J. Zhang, Y.J. Wang, K.Y. Cheuk, A.L.H. Hung, T.P. Lam, Y. Qiu, J.Q. Feng, W.Y.W. Lee, J.C.Y. Cheng, Abnormal lacuno-canalicular network and negative correlation between serum osteocalcin and Cobb angle indicate abnormal osteocyte function in adolescent idiopathic scoliosis, Faseb J. 33(12) (2019) 13882-13892.

[39] M. Mashiatulla, R.D. Ross, D.R. Sumner, Validation of cortical bone mineral density distribution using micro-computed tomography, Bone 99 (2017) 53-61.

[40] M. Firbank, A. Coulthard, R. Harrison, E. Williams, A comparison of two methods for measuring the signal to noise ratio on MR images, Physics in medicine and biology 44(12) (1999) N261.

[41] B.R. McCreadie, S.J. Hollister, M.B. Schaffler, S.A. Goldstein, Osteocyte lacuna size and shape in women with and without osteoporotic fracture, Journal of Biomechanics 37(4) (2004) 563-572.

[42] F.L. Bach-Gansmo, A. Bruel, M.V. Jensen, E.N. Ebbesen, H. Birkedal, J.S. Thomsen, Osteocyte lacunar properties and cortical microstructure in human iliac crest as a function of age and sex, Bone 91 (2016) 11-19.

[43] M.P. Akhter, D. Kimmel, J. Lappe, R. Recker, Effect of Macroanatomic Bone Type and Estrogen Loss on Osteocyte Lacunar Properties in Healthy Adult Women, Calcified Tissue International (2017) 1-12.

[44] M. Stauber, R. Müller, Volumetric spatial decomposition of trabecular bone into rods and plates - A new method for local bone morphometry, Bone 38(4) (2006) 475-484.

[45] A. Carriero, M. Doube, M. Vogt, B. Busse, J. Zustin, A. Levchuk, P. Schneider, R. Müller, S.J. Shefelbine, Altered lacunar and vascular porosity in osteogenesis imperfecta mouse bone as revealed by synchrotron tomography contributes to bone fragility, Bone 61 (2014) 116-124.

[46] P. Milovanovic, B. Busse, Inter-site Variability of the Human Osteocyte Lacunar Network: Implications for Bone Quality, Curr Osteoporos Rep (2019).

[47] H. Hemmatian, M.R. Laurent, S. Ghazanfari, D. Vanderschueren, A.D. Bakker, J. Klein-Nulend, G.H. van Lenthe, Accuracy and reproducibility of mouse cortical bone microporosity as quantified by desktop microcomputed tomography, Plos One 12(8) (2017).

[48] M.L. Bouxsein, S.K. Boyd, B.A. Christiansen, R.E. Guldberg, K.J. Jepsen, R. Müller, Guidelines for assessment of bone microstructure in rodents using micro-computed tomography, J Bone Miner Res 25(7) (2010) 1468-86.

[49] E.N. Cresswell, T.M. Nguyen, M.W. Horsfield, A.J. Alepuz, T.A. Metzger, G.L. Niebur, C.J. Hernandez, Mechanically induced bone formation is not sensitive to local osteocyte density in rat vertebral cancellous bone, J Orthop Res (2017).

[50] A. Levchuk, P. Schneider, M. Meier, P. Vogel, F. Donaldson, R. Müller, An Automated Step-Wise Micro-Compression Device for 3D Dynamic Image-Guided Failure Assessment of Bone Tissue on a Microstructural Level Using Time-Lapsed Tomography, Frontiers in Materials 5 (2018) 14.

[51] S.M. Tommasini, A. Trinward, A.S. Acerbo, F. De Carlo, L.M. Miller, S. Judex, Changes in intracortical microporosities induced by pharmaceutical treatment of osteoporosis as detected by high resolution micro-CT, Bone 50(3) (2012) 596-604.

[52] B.A.a.R.M. E. Goff, A novel shape filter for lacunar imaging in human bone using ultra-high-resolution desktop micro-CT, in: M.O. P. Nithiarasu, and M. Oshima (Ed.) 6th International Conference on Computational and Mathematical Biomedical Engineering (CMBE 2019), Sendai City, Japan, 2019, pp. 651-654.

646 [53] J. Sijbers, A. Postnov, Reduction of ring artefacts in high resolution micro-CT reconstructions,
647 Physics in Medicine and Biology 49(14) (2004) N247-N253.

648

SUPPLEMENTARY DOCUMENT

Below are several figures which provide additional information regarding the specifics of the imaging methodology.

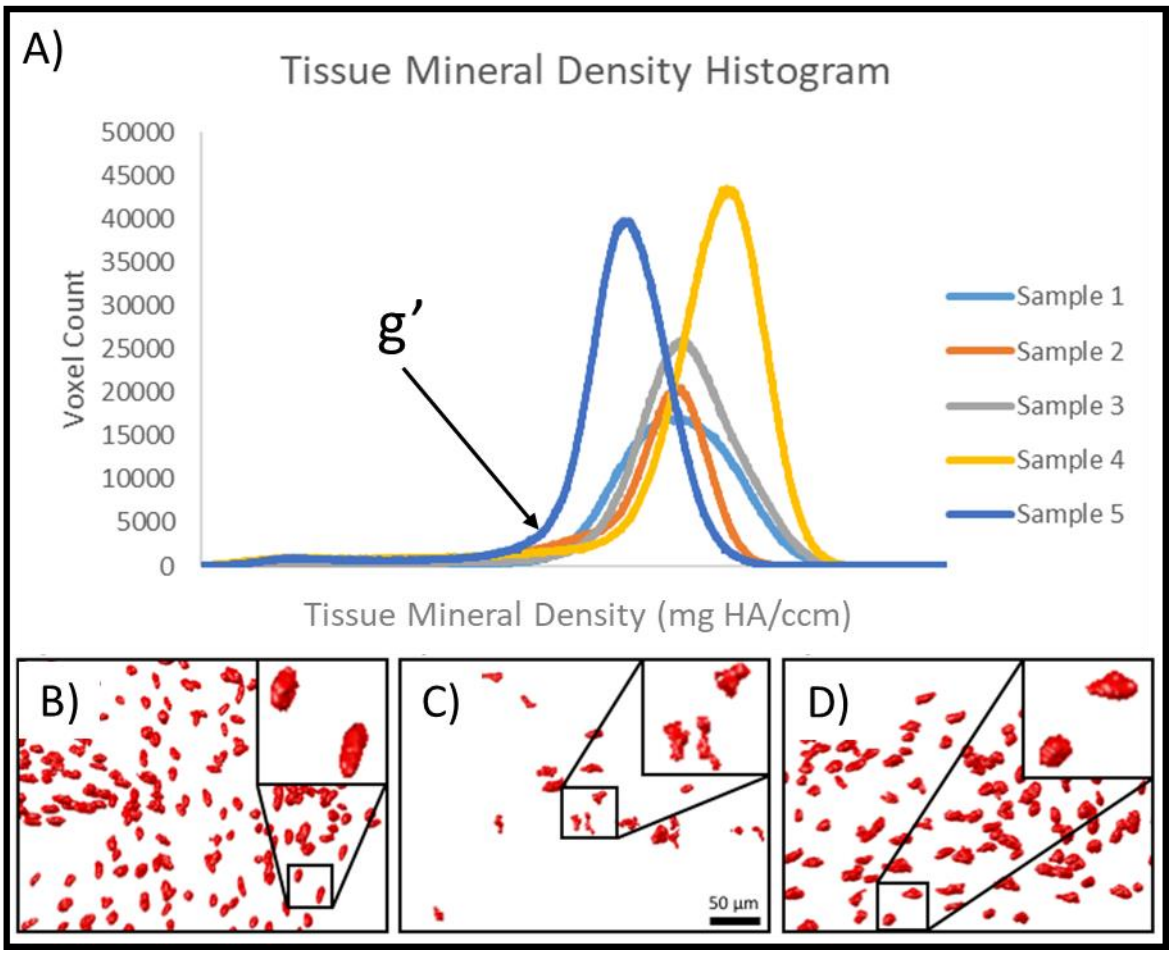

Figure S1: A) TMD histograms for several samples where g' is the critical point. B) Segmented lacunae using a fixed threshold applied to sample 1. C) Segmented lacunae using the same fixed threshold that was applied to sample 1 to sample 2. D) Individualized threshold approach (g') calculated for sample 2 and the resulting segmented lacunae.

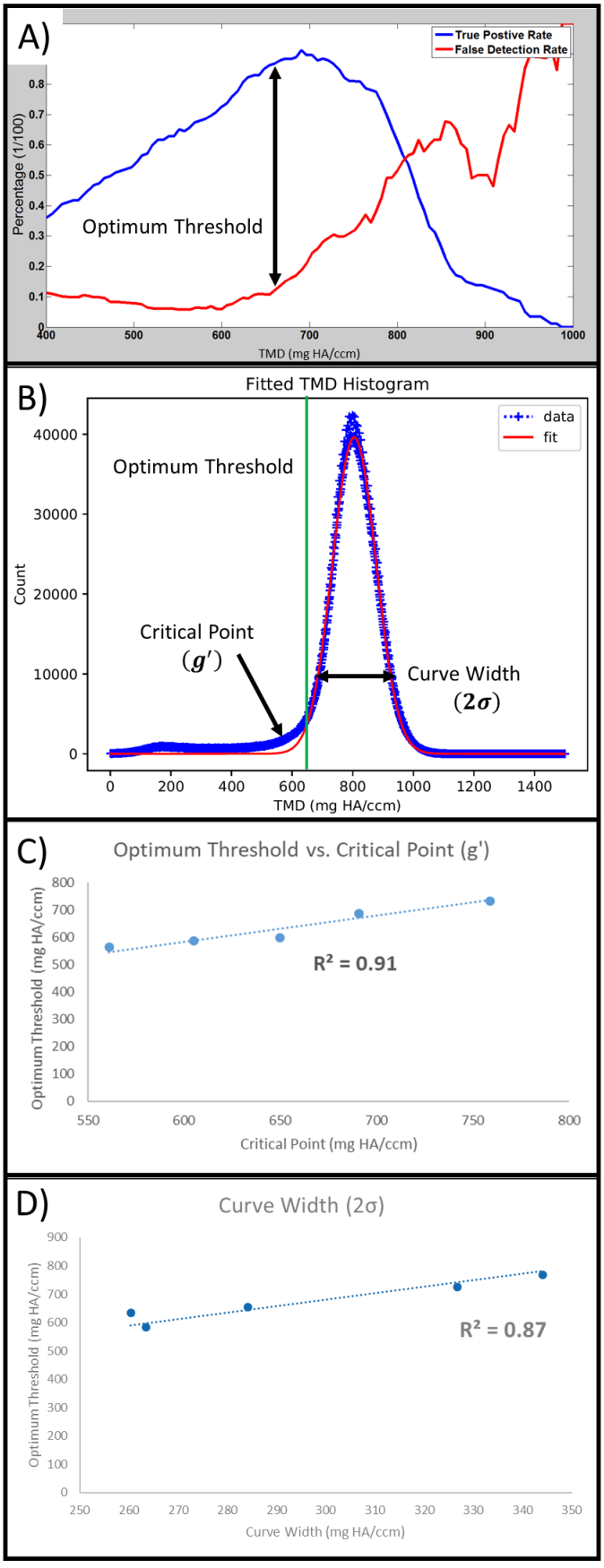

Figure S2: Individualized threshold selection. A) Iterative application of many single thresholds and each compared with the manual segmentation 3D coordinates of a given image subregion. Optimum threshold was defined as the single threshold

659 *that maximized the true positive rate and minimized the false detection rate. B) Typical TMD histogram of the bone biopsy's*
660 *micro-CT image. Optimum threshold (green) determined from (A) and the distribution characteristics including the critical*
661 *point (g') and curve width (2sigma) were calculated from the Gaussian fit of the data. C) Correlation between the optimum*
662 *threshold for each of the five manually segmented subregions and the corresponding critical point (g') from each respective*
663 *TMD histogram. D) Correlation between the optimum threshold for each of the five manually segmented subregions and the*
664 *corresponding distribution width (2sigma) from each respective TMD histogram.*

665

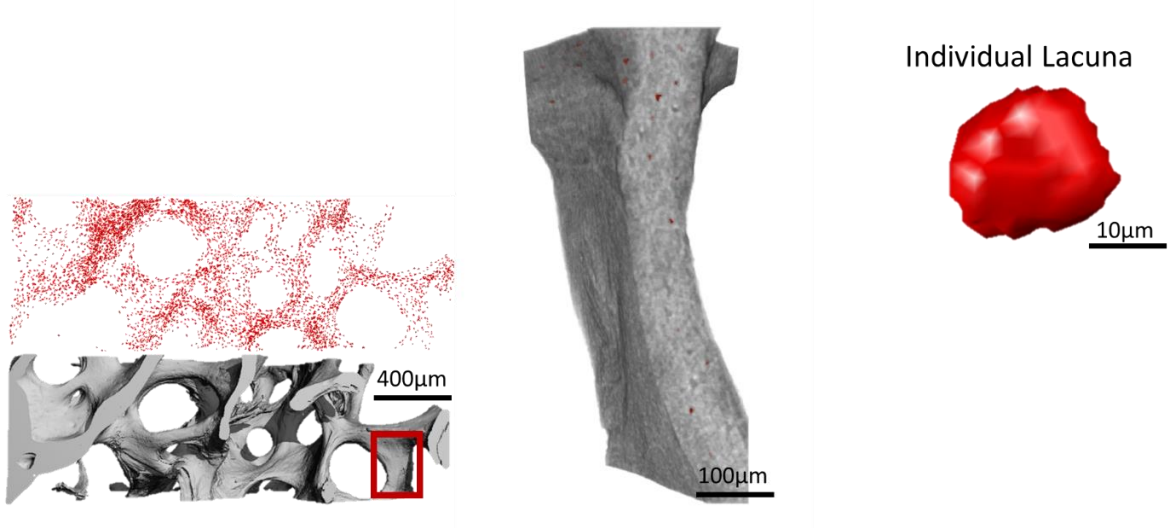

666

667 *Figure S3: Animation of lacunar segmentation from the tissue level down to the individual cell level (see powerpoint file).*